

Micrometeoroid Impact Rate Analysis for an Artemis-Era Lunar Base

2 DANIEL A. YAHALOMI,^{1,2,*} MATTHEW T. SCOGGINS,¹ NASIAH ANDERSON,^{3,†} MARK DRIKER,^{3,‡} KOKORO ONUMA,^{3,†}
3 KWAMENA T. AWOTWI,⁴ JUSTIN M. DONOVAN,⁴ PRIYAN SATHIANATHAN,⁴ AND MICHAEL J. MASSIMINO⁵

4 ¹Department of Astronomy, Columbia University, 550 W 120th St., New York NY 10027, USA

5 ²Center for Computational Astrophysics, Flatiron Institute, 162 Fifth Ave, New York, NY 10010, USA

6 ³Columbia Secondary High School, 425 W 123rd Street, New York NY 10027, USA

7 ⁴Columbia University, 550 W 120th St., New York NY 10027, USA

8 ⁵Department of Mechanical Engineering, Columbia University, 500 W. 120th St., New York NY 10027, USA

ABSTRACT

10 The National Aeronautics and Space Administration's (NASA) Artemis Mission aims to return astronauts to the Moon and establish a base at the South Pole. Ensuring the safety of long-duration habitation requires understanding the threat of meteoroid and micrometeoroid impacts. While meteoroid fluxes are well characterized by ground- and space-based observations, micrometeoroids are too small for current monitoring and will impact the lunar surface directly. Using NASA's Meteoroid Engineering Model 3.0 (MEM 3), we estimate micrometeoroid impact rates on a base comparable in size to the International Space Station, with assumed dimensions of 100 m × 100 m × 10 m. We find that the lunar poles experience ∼1.6 times fewer impacts than the equator. We show that a lunar base would be subjected to ∼15,000–23,000 impacts per year, depending on its location on the lunar surface – with minima at the lunar poles. To assess the mitigating effect of protection systems, we develop a functional relationship describing the number of impacts that penetrate the shielding as a function of the maximum meteoroid mass the shield can arrest. We estimate that the use of state-of-the-art Whipple shields will protect against ∼99.9997% of impacting micrometeoroids. By running the MEM 3 simulations with a minimum mass equal to the critical mass of modern Whipple shields, we determine that a shielded lunar base would be subjected to ∼0.024–0.037 impacts per year, depending on its location on the lunar surface – again with minima at the poles. These results indicate that the [1] lunar poles are optimal locations for sustained habitation and [2] that current shielding technology can reduce micrometeoroid threats by nearly five orders of magnitude making long-duration lunar habitation very feasible.

1. BACKGROUND AND MOTIVATION

30 The Artemis program, led by National Aeronautics and Space Administration's (NASA), marks a renewed commitment to sustained human presence on the Moon. Building upon the legacy of Apollo, Artemis aims not only to return astronauts to the lunar surface but also to establish a long-term base of operations at the lunar south pole. This initiative, in collaboration with international and commercial partners, envisions a new era of lunar exploration that will serve as a stepping stone for missions to Mars and beyond. As planning for sur-

40 face infrastructure advances, assessing the environmental risks faced by long-duration lunar assets becomes critical.

43 Key to this vision is the *Artemis Base Camp* architecture. The base camp concept frames how future landers, habitats, logistics, and operations might evolve on the lunar surface. To design for longevity, one must account for the myriad environmental hazards that a long-duration outpost will face — among them radiation, extreme thermal cycling, regolith dynamics, seismic shaking, dust, and, of particular importance to this work, meteoroid impacts.

52 Artemis III, currently planned for ∼2027, will be an exploratory mission to the lunar south pole, providing reconnaissance for future sustained surface operations. NASA has identified the south polar region—specifically the *Artemis Exploration Zone* (AEZ)—as

Corresponding author: Daniel A. Yahalom
daniel.yahalom@columbia.edu

* Flatiron Research Fellow

† Columbia STAR Program Student

the prime target due to its scientific value and proximity to Permanently Shadowed Regions (PSRs) that may contain accessible water ice (Peña-Asensio et al. 2024). Building on this framework, Peña-Asensio et al. (2024) used a multi-criteria decision analysis to identify the Nobile Rim region as a leading candidate for the Artemis III landing site. The selection criteria encompass features such as stable, flat terrain to ensure safety during landing and operations; unobstructed communication links with Earth to facilitate effective data transfer and mission management; sufficient solar illumination to support power generation; and environmental conditions that keep equipment within acceptable temperature ranges—all aimed at achieving the highest possible scientific yield (Peña-Asensio et al. 2024).

While landing site selection focuses on ensuring the safety and scientific value of surface operations, long-term mission success will also depend on protecting habitats, vehicles, and equipment from the harsh lunar environment. One critical consideration in this context is shielding against micrometeoroid and orbital debris (MMOD) impacts, which pose a persistent hazard to both crewed and uncrewed systems.

1.1. Current MMOD Shielding

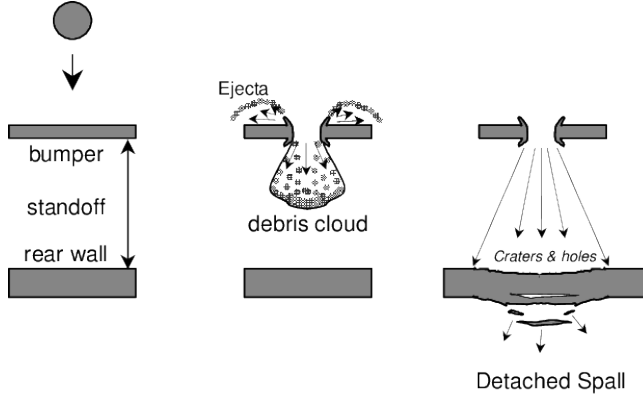


Figure 1. Whipple shield schematic from Ryan et al. (2015).

In establishing a Lunar Base as a part of the Artemis Mission, there will inevitably be some meteoroid shielding protocol. The specific shielding plans for the Artemis mission are not yet known; however, reasonable inferences can be made based on NASA's current Micrometeoroid and Orbital Debris (MMOD) shielding designs. The classic MMOD shield (Whipple shield) is composed of a thin sacrificial bumper and a rear wall, with some interior spacing Christiansen et al. (2009) typically constructed of aluminum (Christiansen et al. 2009). Such a configuration is shown in Figure 1. Assuming that NASA will use a Whipple shield made of aluminum

throughout the Artemis mission, we can estimate the minimum size of a projectile that would be capable of breaking through the shield. We can use the equation for critical diameter for a Whipple shield, in high velocity space, as presented in Ryan & Christiansen (2010), and shown below:

$$d_c = 3.918 F_2^* \frac{t_w^{2/3} S^{1/3} (\sigma/70)^{1/3}}{\rho_p^{1/3} \rho_b^{1/9} (V \cos \theta)^{2/3}}. \quad (1)$$

Assuming the projectile is a solid sphere of density ρ_p , the mass is:

$$m_c = \frac{\pi}{6} \rho_p d_c^3 \quad (2)$$

Substituting Equation (1) into the expression for mass, we can determine the critical mass of micrometeoroid impactor:

$$m_c = \frac{\pi}{6} (3.918 F_2^*)^3 \frac{t_w^2 S (\sigma/70)}{\rho_b^{1/3} (V \cos \theta)^2}. \quad (3)$$

Here, F_2^* is the projectile fragmentation efficiency, t_w is the thickness in cm of the rear wall, S is the spacing in cm of the rear wall, σ is the rear wall yield stress in ksi, ρ_p is the density of the projectile, ρ_b is the density of the front bumper, V is the velocity of the projectile, and θ is the angle of impact. Using this equation and representative parameter values (see e.g., Ryan & Christiansen (2010)), a back-of-the-envelope calculation for the fastest micrometeoroids – with velocities up to 72 km/s – yields a critical shield diameter of approximately 0.12 cm. This value should be regarded as an order-of-magnitude estimate, indicating that objects larger than roughly 0.12 cm in diameter may exceed the protective capability of state-of-the-art MMOD shields. This underscores the importance of precise and accurate modeling of the micrometeoroid environment.

We note that NASA may ultimately employ novel shielding strategies – such as the use of lunar regolith in shielding, which will be abundant on the surface – no specific plans or experimental data on their performance have yet been disclosed. Accordingly, in what follows we proceed under the assumption of a Whipple-type shielding configuration as a representative baseline.

1.2. Current Lunar Impact Monitoring

Current lunar impact monitoring techniques employ several complementary observational strategies, each with distinct strengths and limitations. These include topographic mapping through laser altimetry, detection of impact-induced optical flashes on the lunar surface, and temporal imaging of newly formed craters. Collectively, these methods have greatly advanced our under-

standing of the lunar impact environment, particularly within the meteoroid size regime where optical and morphological signatures are more readily detectable. However, despite their demonstrated success in characterizing larger impact events, these techniques typically lack the sensitivity required to systematically monitor or constrain impacts in the micrometeoroid regime. As noted by Speyerer et al. (2016b), “although studies of existing craters and returned samples offer insight into the process of crater formation and the past cratering rate, questions still remain about the present rate of crater production.”

- **Temporal Imaging:** The Lunar Reconnaissance Orbiter Camera (LROC), launched in 2009, captures high-resolution images of the Moon’s surface, enabling the detection of new impact craters through temporal image comparisons. Speyerer et al. (2016a) identified over 200 new craters, with a resolution limit of approximately 10 meters. Laboratory experiments and dimensional analyses show that crater size depends on impactor size, velocity, gravity, and material properties in a well-characterized scaling framework (Melosh 1989; Holsapple 1993). For meteor impactors striking the lunar surface at typical impact velocities, the final crater diameter is typically \sim 10–20 times larger than the projectile diameter. Thus, the LROC temporal imaging data is sensitive to craters corresponding to meteors roughly 0.5 to 1 meters in diameter. Therefore, this technique is insensitive to smaller, micrometeoroid impacts and is additionally limited by the availability and cadence of suitable image pairs

- **Flash Detection:** Earth-based telescopes monitor the Moon’s nearside hemisphere for brief optical flashes produced by hypervelocity meteoroids striking the lunar surface. Observations are constrained to nighttime, favorable weather, and specific lunar phases when illumination is less than 50%, which optimize contrast against the dark background. The observed flash brightness, often modeled as black-body emission, is assumed to represent a fraction (the luminous efficiency) of the impactor’s kinetic energy; with an estimate of impact velocity, this enables derivation of the meteoroid’s mass and size. Over the past decades, this technique has allowed determination of the flux and size distribution of small near-Earth objects in the centimeter regime (Madiedo et al. 2014; Avdellidou & Vaubaillon 2019). The Lunar Meteoroid Impact Observer (LUMIO) is a CubeSat

scheduled to launch in 2027 in order to observe the lunar farside for light flashes produced by impacts. By operating at the Earth–Moon L2 point, LUMIO’s observations are not limited by weather and it eliminates noise from Earth-shine (Cipriano et al. 2018). LUMIO’s primary science goal is to answer “*what are the spatial and temporal characteristics of meteoroids impacting the Lunar surface?*” and its sensitivity will extend into the micrometeoroid regime (Cervone et al. 2022).

- **Topographic Mapping:** The Lunar Orbiter Laser Altimeter (LOLA) measures elevation changes on the lunar surface via laser altimetry to detect large-scale impact events. LOLA performs optimally in characterizing the topography at the poles where the LRO orbits converge. While highly accurate for broader terrain mapping, LOLA’s spatial resolution limits detection to craters larger than approximately 300–400 meters. Via typical impact scaling relations, these craters suggest minimum impactor sensitivity on the order of 15–40 meters. This makes it currently unsuitable for tracking the small-scale micrometeoroid environment for Artemis-era lunar surface operations (Smith et al. 2010; Keresztsuri 2022).

These constraints collectively highlight the need for more sensitive modeling of the lunar surface prior to the establishment of a long-term lunar base and long-term human presence on the Moon.

1.3. NASA’s Meteoroid Engineering Model (MEM 3)

NASA’s Meteoroid Engineering Model version 3 (MEM 3) is the agency’s current physics-based model of the inner-solar-system meteoroid environment (McNamara et al. 2004; Moorhead 2020). Given a user-specified, time-dependent trajectory, MEM 3 returns velocity-resolved, directional fluxes and a bulk-density distribution for meteoroids in the mass range $10^{-6} – 10^1$ grams encountered along that path, explicitly accounting for *gravitational focusing* and *planetary shielding* near major bodies – Earth, Moon, Mercury, Venus, and Mars (Moorhead 2020). These features are essential when translating interplanetary fluxes to the near-Moon environment, where local gravity from the Earth perturbs meteoroid trajectories and the solid body of the Earth occludes part of the sky.

Compared to prior MEM releases, MEM 3 improves the correlation between impact direction and speed, incorporates a bulk-density distribution, updates sporadic source populations, and provides both GUI and command-line interfaces for efficient mission analyses

(Moorhead 2020; Moorhead et al. 2020b). Model behavior and predicted impact rates have been compared against spacecraft records (e.g., LDEF; Pegasus II/III), demonstrating good agreement – within a factor of 2–3 of the MEM 3 prediction (Moorhead et al. 2020b).

Although MEM 3 is often used for Earth-orbiting satellites and interplanetary cruise phases, its directional, velocity-dependent outputs are applicable to a fixed lunar installation by treating the habitat as a “spacecraft” with a stationary state vector on the Moon’s surface. In that configuration, MEM 3 provides the incident flux as a function of local time and look direction at the site of interest, thereby enabling *site-specific* penetration and damage-risk assessments. Beyond engineering usage, MEM-based flux predictions have been leveraged in planetary science contexts (e.g., interpreting Bennu’s particle-ejection events), demonstrating the model’s relevance to the near-Earth micrometeoroid population (Bottke et al. 2020).

2. METHODS

Each run of the MEM 3 code provides outputs for one lunar base. To derive the impact rate across the full surface of the moon, we draw 1,000 points from a Fibonacci sphere to create the initial locations of our lunar base, in selenographic coordinates, described by ϕ measured from the lunar north pole and θ measured from the Moon’s prime meridian. Sampling the Fibonacci sphere distributes the bases evenly across the moon’s surface, with a ϕ distribution that is approximately normal and a uniform θ distribution.

All trajectories start at J2000, or the J~2451544 Julian date, with $\theta = 0$ pointing towards the vernal equinox. We calculate the trajectory of the lunar base for the draconic period of the moon $T = 27.2122$ days, and calculate 30 snapshots of the lunar base over this period for the trajectory file. MEM 3 allows the coordinate system to be centered on the moon, in either ecliptic or equatorial coordinates. We choose to run the simulations in an ecliptic coordinate frame, which requires a transformation of our selenographic coordinates. Given the initial base location in selenographic coordinates, $L(t_0) = [\phi_0, \theta_0]$, defined by ϕ_0 and θ_0 at time J2000, t_0 , the location at a later time t can be estimated as $L(t) = [\phi_0, \theta_0 + \omega(t - t_0)]$ for angular velocity $\omega = 2\pi/T$. This location is then converted into Cartesian coordinates, $L(t) = [x, y, z]$. The velocity at a given surface location is calculated as the rotational velocity of the base due to the Moon’s rotation. The velocity vector is given by

$$\mathbf{v}(t) = \frac{V}{|r_{xy}|} [-y, x, 0], \quad (4)$$

where

$$V = \omega r_{\text{moon}} \sin(\phi_0), \quad (5)$$

and

$$|r_{xy}| = \sqrt{x^2 + y^2}. \quad (6)$$

for moon radius r_{moon} . With the base location in Cartesian coordinates and the bases’ velocity, we then transform these into the ecliptic by rotating the coordinate system by the moon’s obliquity relative to the ecliptic plane, a rotation of $\sim 1.54^\circ$. This is an approximation that ignores the libration of the moon, which can be up to 7° . This means our base locations can be off by as much as 200 km, which is on the order of the separation between our simulated base locations.

MEM 3 outputs the flux files with a directional dependent flux. We choose to center our output origin to the moon, and use the body-fixed axes. In the body-fixed system, the \hat{x}_+ direction is always the direction of motion of the spacecraft (in our case, the direction that the moon is rotating, counterclockwise in the ecliptic plane), and \hat{y}_+ is determined by the cross product of \hat{r} , the radial vector relative to the moon’s center, with \hat{x}_+ . \hat{z}_+ is then the cross product of \hat{x}_+ and \hat{y}_+ , meaning \hat{z}_+ will always point in the radial direction, directly away from the surface of the moon. This can be seen in Figure 2.

MEM 3 simulates two distinct meteoroid populations: a higher-density component and a lower-density component, denoted here by F_α and F_β , respectively. Within each population, the density is assumed independent of speed, direction, and mass. For a given lunar base, the total flux is computed as the sum of contributions from both populations.

The MEM 3 model outputs fluxes in units of $\text{m}^{-2} \text{yr}^{-1}$. To facilitate comparison with the total flux incident on a specific structure, we convert these to units of impacts per lunar base per year by scaling with the surface area of the base along each plane of impact. Assuming a lunar base roughly the size of the International Space Station, we take its height, length, and width to be

$$h = 10 \text{ m}, \quad l = 100 \text{ m}, \quad w = 100 \text{ m}.$$

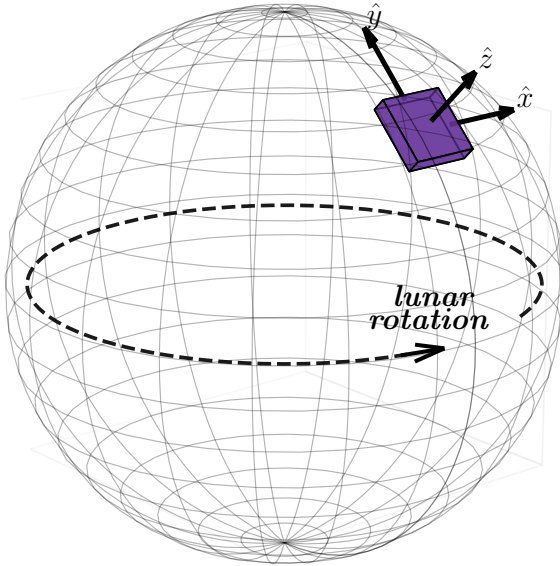
The total flux from the higher-density population at a specific selenographic initial location defined by ϕ_0, θ_0 at J2000 is then

$$\begin{aligned} F_\alpha(\phi_0, \theta_0) &= lw [F_{\alpha,z+}(\phi_0, \theta_0)] \\ &\quad + lh [F_{\alpha,x+}(\phi_0, \theta_0) + F_{\alpha,x-}(\phi_0, \theta_0)] \\ &\quad + lh [F_{\alpha,y+}(\phi_0, \theta_0) + F_{\alpha,y-}(\phi_0, \theta_0)], \end{aligned} \quad (7)$$

where $F_{\alpha,i\pm}(\phi_0, \theta_0)$ denotes the higher-density flux incident from the $\pm i$ direction, with $i \in x, y, z$, expressed in $\text{m}^{-2}, \text{yr}^{-1}$ and integrated over all velocities.

MEM3 Coordinate System and Lunar Base

Lunar Surface



(Assumed Lunar Base size: width: 100m, length: 100m, height: 10m)

Zoom-in on Lunar Base

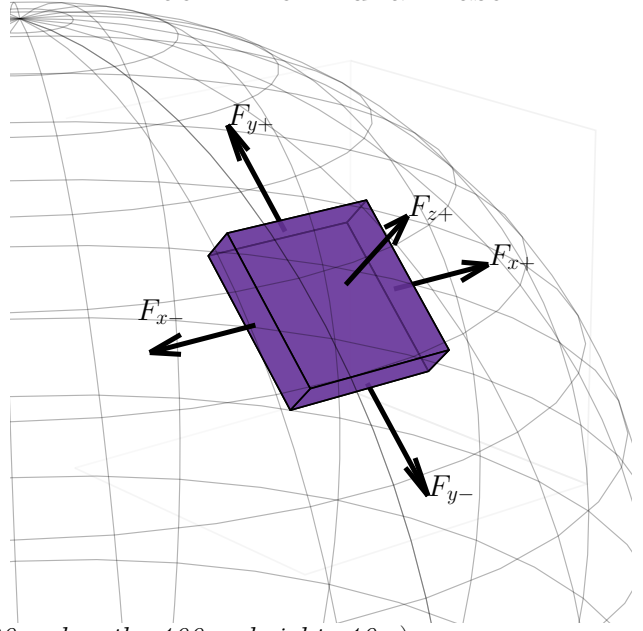


Figure 2. Schematic showing coordinate system used in the MEM 3 simulations.

Analogously, the total flux from the lower-density population is

$$\begin{aligned} F_\beta(\phi_0, \theta_0) = & lw [F_{\beta,z+}(\phi_0, \theta_0)] \\ & + lh [F_{\beta,x+}(\phi_0, \theta_0) + F_{\beta,x-}(\phi_0, \theta_0)] \\ & + lh [F_{\beta,y+}(\phi_0, \theta_0) + F_{\beta,y-}(\phi_0, \theta_0)]. \end{aligned} \quad (8)$$

Finally, the total meteoroid flux incident on the lunar base, in units of impacts per year per base, is

$$F_{\text{tot}}(\phi_0, \theta_0) = F_\alpha(\phi_0, \theta_0) + F_\beta(\phi_0, \theta_0). \quad (9)$$

3. RESULTS & DISCUSSION

3.1. Unshielded Impact Rate

The MEM 3 model allows the user to specify the minimum meteoroid particle mass, within the range 10^{-6} – 10 g. As an initial case, we simulate an *unshielded impact rate* by including the full range of meteoroid masses in MEM 3. This configuration represents the impact flux that a lunar base would experience in the absence of any protective shielding. While this assumption is physically unrealistic—since even minimal structural materials would provide *some* degree of protection—it serves as a useful baseline from which to quantify the relative benefits of shielding in subsequent analyses.

As previously described, we simulate 1,000 points evenly distributed across the lunar surface as a Fibonacci sphere. This gives a set of discrete impact rates

on the lunar surface. To obtain a continuous representation of meteoroid impact rates across the lunar surface, we interpolate the results of these 1,000 discrete MEM 3 simulations sampled at different selenographic latitudes and longitudes. The interpolation is performed using a radial basis function (RBF) scheme implemented in the SciPy library (Virtanen et al. 2020a). In this approach, each simulated point (ϕ_i, θ_i) , corresponding to latitude and longitude, is associated with a total impact rate F_i derived from MEM 3. The function constructs a two-dimensional interpolant

$$F_{\text{interp}}(\phi, \theta) = \sum_{i=1}^N w_i \varphi(r_i), \quad (10)$$

where $r_i = \sqrt{(\phi - \phi_i)^2 + (\theta - \theta_i)^2}$ is the great-circle distance (in degrees) between evaluation and sample points, $\varphi(r_i)$ is the chosen radial basis function, and w_i are the weights obtained by solving the linear system enforced by the known values F_i .

We employ the “multiquadric” kernel,

$$\varphi(r) = \sqrt{1 + (\epsilon r)^2}, \quad (11)$$

which provides smooth global interpolation suitable for data on a spherical surface. A small smoothing factor (`smooth=1`) is applied to mitigate overfitting due to local fluctuations in the discrete model output.

This results in the impact rate maps shown in Figure 3 and Figure 4 – for Mollweide and polar projections, respectively. The sub-Earth point (“x”) on the lunar surface was computed at the J2000 epoch using **Astropy** ([Astropy Collaboration et al. 2013, 2018, 2022](#)) with the DE432s ephemeris. The barycentric positions of the Earth and Moon were used to form a Moon–Earth vector in the ICRS frame, from which the sub-Earth longitude was obtained via $\theta = \tan^{-1}(y/x)$ and wrapped to $[-180^\circ, +180^\circ]$ for Mollweide map projection compatibility. Three key trends emerge from this “unshielded” lunar base impact rate map: (1) impact rates are high, ranging from approximately 15,000 to 23,000 impacts per year depending on base location; (2) the lunar poles experience systematically fewer impacts than the equatorial regions; and (3) Earth’s gravitational focusing dominates over its shielding effect, with the maximum impact rate occurring at the sub-Earth longitude (see [Moorhead et al. \(2020a\)](#) for further discussion of planetary gravitational focusing of meteor streams).

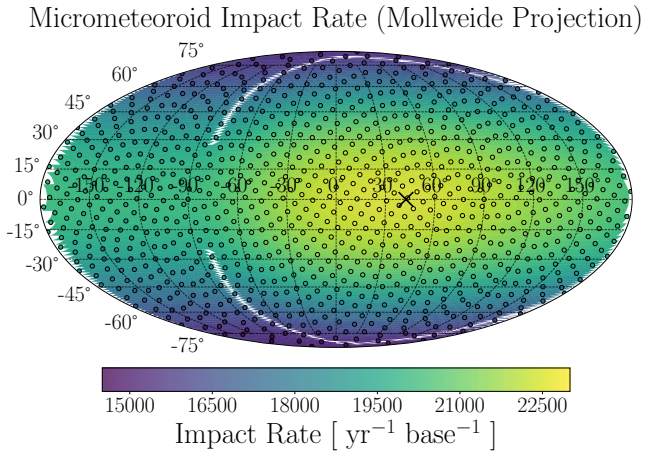


Figure 3. Mollweide projection of “unshielded” impact rate of micrometeoroids on the lunar surface – i.e., complete 10^{-6} – 10 g mass range in **MEM 3**. The “x” on the map represents the sub-Earth point on the lunar surface.

3.2. Shielded Impact Rate

As discussed previously, the performance of a meteoroid shield can be characterized by its *critical mass*, m_c (Equation 3), defined as the maximum projectile mass that the shield can prevent from penetrating. To evaluate this parameter, we adopt a conservative approach to the ballistic limit function, selecting input values that minimize the critical mass and thereby represent a worst-case scenario. This ensures that if a shield design is predicted to withstand an impact, the assessment

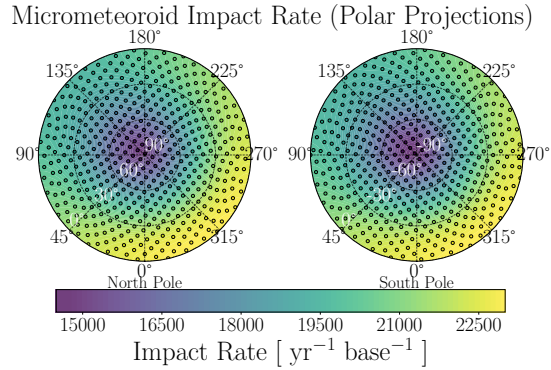


Figure 4. Polar projections of “unshielded” impact rate of micrometeoroids on the lunar surface – i.e., complete 10^{-6} – 10 g mass range in **MEM 3**.

remains robust under the most adverse, but possible, conditions.

For simplicity, we assume $F_2^* = 1$, which is appropriate for projectiles below the critical diameter of a Whipple shield (see [Ryan & Christiansen 2010](#)). We further assume a normal incidence angle ($\theta = 0$) to yield the smallest critical diameter. Additional parameters are adopted from [Ryan & Christiansen \(2010\)](#): rear wall thickness $t_w = 0.48$ cm, bumper density $\rho_b = 2.851$ g cm $^{-3}$, rear wall yield stress $\sigma = 52$ ksi, and rear wall spacing $S = 11.43$ cm.

Meteoroids are composed primarily of silicate minerals (Si and O), though metallic constituents such as Fe and Ni are also common ([Jessberger et al. 1988; Love & Brownlee 1993; Flynn et al. 2016](#)). To maintain a conservative estimate of impact severity, we assume a nickel composition for the projectile, corresponding to a density of $\rho_p = 8.90$ g cm $^{-3}$ ([National Institute of Standards and Technology, PML 2025](#)).

We then are left with the velocity of the impactor as the only remaining parameter in our critical mass equation. For the simulation suite with the lowest minimum particle mass ($m_{\min} = 10^{-6}$ g), we compute the velocity distribution using the **MEM 3** model, weighted by directionality according to the assumed base geometry, and then average the resulting flux over each lunar base location. Our averaged velocity distribution is calculated as the flux from both the high and low density contributions, and is shown in Fig. 5.

From this velocity distribution, we compute the normalized cumulative distribution, which allows us to randomly draw 10^7 samples. Plugging in this distribution into Equation 3 we get a distribution of critical masses based on current Whipple shield capabilities, as shown in Figure 6. The median critical mass of this distribution is $m_{\text{crit}} = 10^{-1.16}$ g.

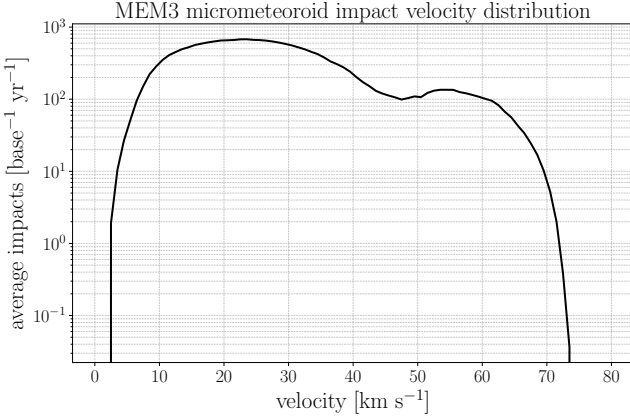


Figure 5. The velocity distribution of impacts for our MEM 3 simulation suite with the minimum mass $m_{\min} = 10^{-6}$ g. This is the averaged velocity distribution across all 1,000 base locations and both high and low density simulations.

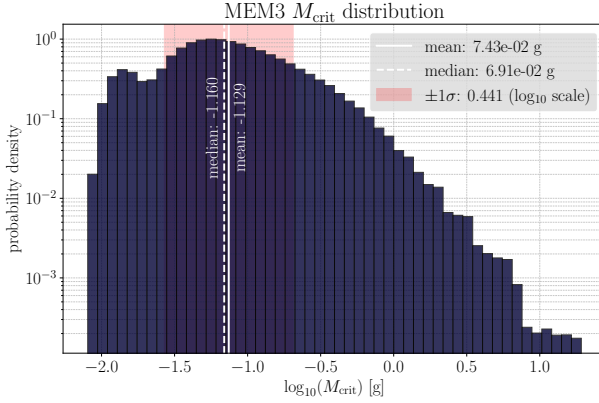


Figure 6. The critical mass distribution of our particles (Equation 3) using the 10^7 samples from the normalized cumulative averaged velocity distribution (Figure 5) and assuming current Whipple shielding capabilities.

We can now evaluate the shielded impact rate in two ways: (1) compare a random sample of impacts from our MEM 3 simulation to the critical mass to determine what fraction of impacts are larger than our median critical mass and (2) re-run the MEM 3 simulation with the minimum mass equal to the median critical mass, $m_{\min} = m_{\text{crit}} = 10^{-1.16}$ g.

The ratio of randomly sampled masses from our mass distribution compared to the derived critical is shown in Figure 7. We find that 99.9997% of these particles have masses below the critical mass. Given that this is calculated with the average velocity distribution, a base on the moon located in an area experiencing fewer than the average number of impacts (i.e. near the poles) and accounting for the fact that most impacts will not be face-on ($\theta > 0$), this implies that current shielding is capable of protecting against nearly every micrometeoroid

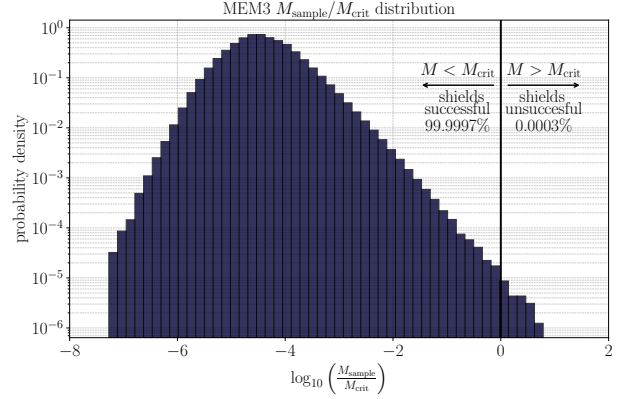


Figure 7. The ratio of randomly sampled masses from our mass distribution compared to the derived critical. We find that the vast majority (> 99.99%) of these impacts are protected by our conservative assumptions for shielding.

impact. Placing a base at the lunar south pole, and assuming that shielding will protect against 99.9997% of the 15,000 annual impacts – we can estimate that there will be ~ 0.045 impacts per base per year. This implies that only once every ~ 22 years will an impact break through Whipple shielding.

We also re-run our full MEM 3 model, as previously described, but with a minimum mass set to the median critical mass, $m_{\min} = m_{\text{crit}} = 10^{-1.16}$ g – yielding the *shielded impact rate*. We reproduce the impact rate map for this “shielded” simulation, as shown in Figure 3 and Figure 9 – for Mollweide and polar projections, respectively. Using this “shielded” simulation, we again find that the lunar poles are impacted systematically less than the equator and that the gravitational focusing from Earth dominates over its planetary shielding as the maximum impact rate occurs at the location of the Earth in the lunar sky. With the updated minimum mass set equal to our estimated critical mass, we find that a lunar base will be impacted ~ 0.024 – 0.037 per year based on its location. At the poles, we estimate that there will be ~ 0.024 impacts per year large enough to break through Whipple shielding or once every ~ 42 years.

3.3. Varying Shielding Capabilities

Using the MEM 3 simulation suite, we can estimate the number of meteoroid impacts at the lunar south pole as a function of the critical shielding diameter. This provides a framework for determining the number of *unshielded* impacts—those that penetrate the protective layers—as a function of the shield’s critical performance threshold. As Artemis-era surface habitat designs mature, such calculations can help identify the critical im-

ielded Micrometeoroid Impact Rate (Mollweide Projec

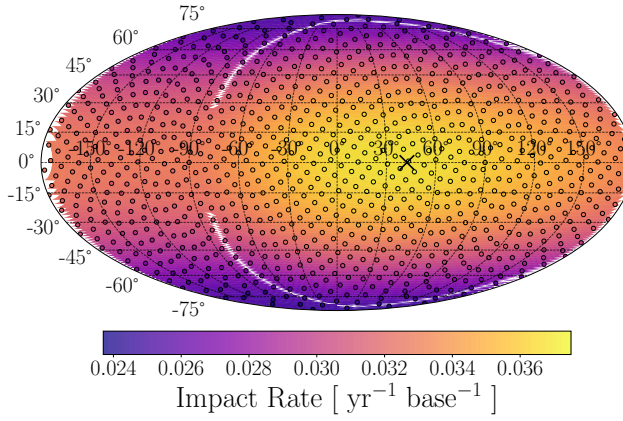


Figure 8. Mollweide projection of “shielded” impact rate of micrometeoroids on the lunar surface – i.e., $10^{-1.16}$ – 10 g mass range in MEM 3. The “x” on the map represents the sub-Earth point on the lunar surface.

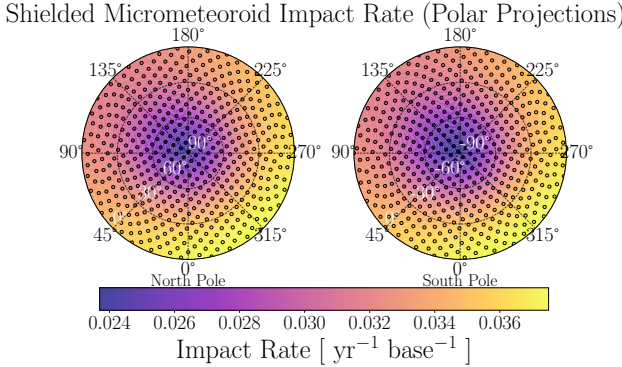


Figure 9. Polar projections of “shielded” impact rate of micrometeoroids on the lunar surface – i.e., $10^{-1.16}$ – 10 g mass range in MEM 3.

500 pact mass or size that shielding must withstand to meet
501 mission safety requirements.

502 To quantify this, we run two additional MEM 3 models
503 with minimum particle masses set to $m_{\min} = 10^{-2}$ g
504 and $m_{\min} = 10^{-4}$ g, complementing our earlier simula-
505 tions at 10^{-6} g and $10^{-1.16}$ g. In total, these four MEM 3
506 simulation sets provide impact fluxes $F(>m|\phi_0, \theta_0)$ for
507 different minimum masses m at a given (ϕ_0, θ_0) loca-
508 tion on the lunar surface. For each run, we calculate
509 the mean impact rate across all locations within 6° of
510 the lunar south pole, representing the expected flux at
511 a notional base site. The resulting mean southern-pole
512 impact rates $F(>m|\phi_{\text{south}}, \theta_{\text{south}})$ are plotted in Fig-
513 ure 10 as a function of their respective MEM 3 limiting
514 mass m .

515 To provide a smooth, physically motivated compari-
516 son, we also compute the expected mass-dependent flux

517 using the semi-empirical Grün relation (Grün et al. 1985;
518 Moorhead 2020), which underlies MEM 3’s baseline inter-
519 planetary meteoroid environment model. The Grün re-
520 lation describes the cumulative flux of meteoroids with
521 mass greater than m (in grams) as

$$F_{\text{Grün}}(>m) = [A(m) + B(m) + C(m)] t_{\text{yr}}, \quad (12)$$

523 where $t_{\text{yr}} = 3.154 \times 10^7$ s is the number of seconds in
524 one year, and

$$A(m) = (c_4 m^{\gamma_4} + c_5)^{\gamma_5}, \quad (13)$$

$$B(m) = c_6 (m + c_7 m^{\gamma_6} + c_8 m^{\gamma_7})^{\gamma_8}, \quad (14)$$

$$C(m) = c_9 (m + c_{10} m^{\gamma_9})^{\gamma_{10}}. \quad (15)$$

528 The empirical coefficients and exponents are

$$c_4 = 2.2 \times 10^3, \quad \gamma_4 = 0.306,$$

$$c_5 = 15, \quad \gamma_5 = -4.38,$$

$$c_6 = 1.3 \times 10^{-9}, \quad \gamma_6 = 2,$$

$$c_7 = 1 \times 10^{11}, \quad \gamma_7 = 4,$$

$$c_8 = 1 \times 10^{27}, \quad \gamma_8 = -0.36,$$

$$c_9 = 1.3 \times 10^{-16}, \quad \gamma_9 = 2,$$

$$c_{10} = 1 \times 10^6, \quad \gamma_{10} = -0.85.$$

536 The Grün relation is evaluated continuously over the
537 range 10^{-6} g < m < 10^1 g. Let $F_{\text{Grün}}(>m_0)$ denote
538 the cumulative Grün flux at the anchor point $m_0 =$
539 10^{-6} g, and $F(>m_0|\phi_{\text{south}}, \theta_{\text{south}})$ the correspond-
540 ing mean southern-pole impact rate from the MEM 3 simu-
541 lation at that mass threshold. We then define a scaled
542 Grün-based model for the impact rate as

$$\frac{F(>m|\phi_{\text{south}}, \theta_{\text{south}})}{F(>m_0|\phi_{\text{south}}, \theta_{\text{south}})} = \frac{F_{\text{Grün}}(>m)}{F_{\text{Grün}}(>m_0)}. \quad (16)$$

544 This scaling preserves the functional shape of the
545 Grün mass-flux relation while normalizing it to the ab-
546 solute impact rate derived from MEM 3 at the south pole
547 – and allows us to predict $F(>m|\phi_{\text{south}}, \theta_{\text{south}})$ for any
548 m . The resulting smoothed relation, shown in Figure 10,
549 provides a continuous estimate of the expected mete-
550 oroid flux as a function of particle mass, which can be
551 directly applied to evaluate shielding performance for
552 various design thresholds.

4. CONCLUSION

554 In this study, we used NASA’s Meteoroid Engineering
555 Model 3 (MEM 3) to quantify the micrometeoroid impact
556 environment across the lunar surface and evaluate its
557 implications for long-duration Artemis-era surface habi-
558 tats. By performing 1,000 directional MEM 3 simulations

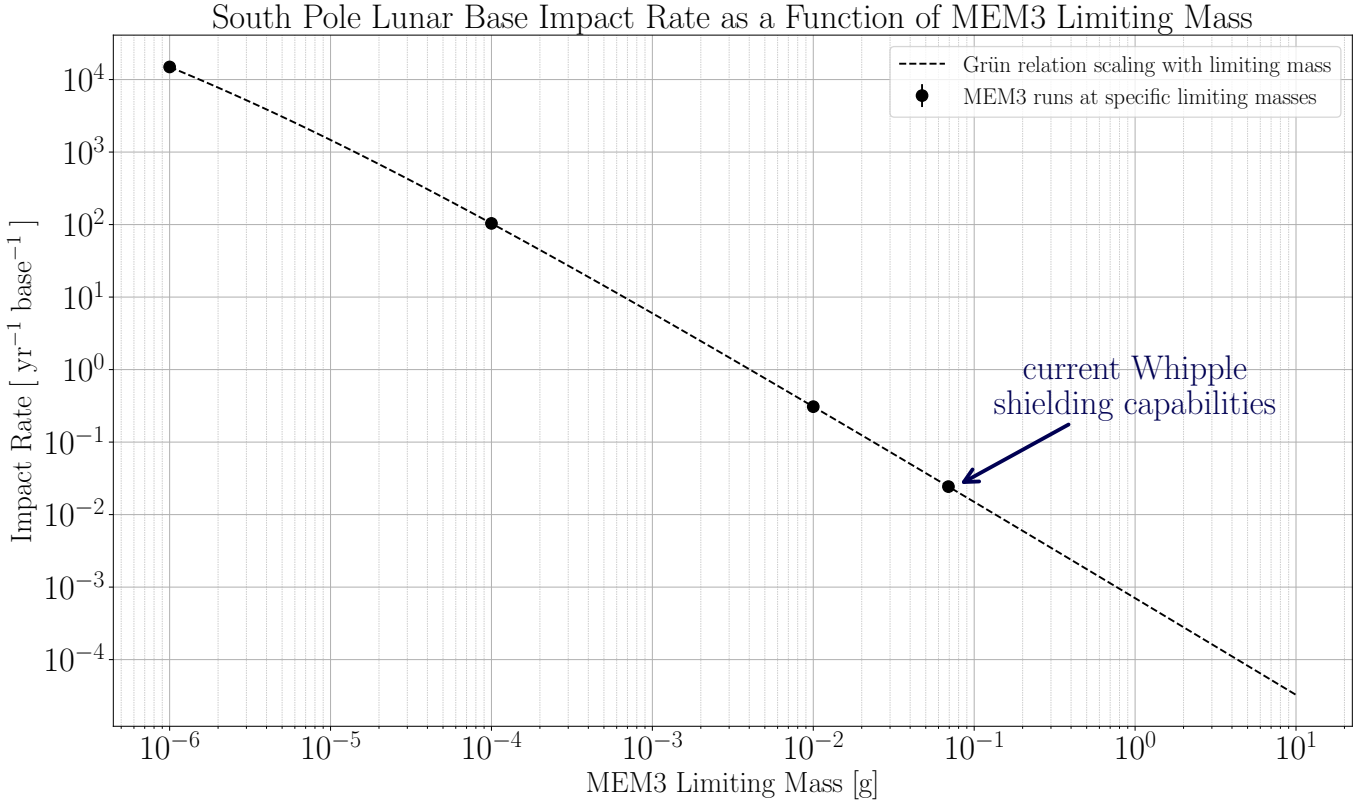


Figure 10. Impact rate on the lunar south pole (mean of simulations within 6° on lunar south pole) as a function of minimum MEM 3 mass. Points represent 4 individual MEM 3 runs with minimum mass set to 10^{-6} , 10^{-4} , 10^{-2} , $10^{-1.16}$ g, respectively. Dashed line shows the Grün relation scaled to the 10^{-6} g minimum mass MEM 3 simulation.

uniformly distributed in selenographic coordinates, we derived both “unshielded” and “shielded” impact rates for a notional lunar base with dimensions comparable to the International Space Station.

Our unshielded simulations indicate that a base of this size would experience approximately 15,000 to 23,000 micrometeoroid impacts per year, with the lunar poles receiving roughly 1.6 times fewer impacts than the equatorial regions. This latitudinal dependence is likely driven primarily by the geometric effects of the Moon’s orientation relative to the meteoroid sources and the partial gravitational focusing of fluxes by Earth.

Using a Whipple-type shield configuration as a conservative baseline, we derived a critical projectile mass of $m_{\text{crit}} \approx 10^{-1.16}$ g. Simulated impactor mass distributions show that approximately 99.9997% of particles fall below this threshold, implying that current MMOD shielding technology can effectively mitigate nearly all micrometeoroid impacts. Accounting for modern Whipple shielding capabilities, we estimate a residual rate of $\sim 0.024\text{--}0.037$ penetrating impacts per year, corresponding to a single unprotected impact event every 27–42 years. We again find that in this regime the lu-

nar poles receive approximately 1.6 times fewer impacts than the equatorial regions.

To extend these discrete simulations, we scaled the empirical Grün meteoroid flux relation to the MEM 3-derived impact rate at $m = 10^{-6}$ g, yielding a smooth function for the expected impact frequency as a function of limiting mass. This approach enables a continuous evaluation of shielding performance across arbitrary design thresholds and provides a practical engineering tool for mission planners.

Overall, our results demonstrate that:

1. The lunar south pole offers a natural reduction in impact risk relative to equatorial sites, supporting its selection for sustained human presence.
2. Existing Whipple shielding technology is sufficient to suppress micrometeoroid hazards by nearly five orders of magnitude, reducing the effective risk to a negligible level for current habitat designs.

Future work should incorporate additional factors such as regolith-based or hybrid shielding materials, transient meteoroid streams, and local topographic effects on flux anisotropy. These refinements will further

improve our understanding of the meteoroid threat environment for upcoming Artemis surface missions and long-term lunar infrastructure.

N.A., M.D., and K.O. were supported by the Student Training in Astronomy Research (STAR) program at Columbia University, which is grateful for the support of the Pinkerton Foundation, New York City Science Research Mentoring Consortium, and the National Os- terbrock Leadership Program of the AAS.

D.A.Y. acknowledges support from NASA Grant #80NSSC21K0960.

D.A.Y. acknowledges support from the NASA/NY Space Grant

D.A.Y. thanks the LSST-DA Data Science Fellowship Program, which is funded by LSST-DA, the Brinson Foundation, and the Moore Foundation; his participation in the program has benefited this work.

This work made use of the following software packages: `astropy` (Astropy Collaboration et al. 2013, 2018, 2022), `matplotlib` (Hunter 2007), `numpy` (Harris et al. 2020), `python` (Van Rossum & Drake 2009), and `scipy` (Virtanen et al. 2020b; Gommers et al. 2025).

Software citation information aggregated using The Software Citation Station (Wagg & Broekgaarden 2024; Wagg et al. 2025).

`ChatGPT` was utilized to improve wording at the sentence level and assist with coding inquires – last accessed in 2025 October.

REFERENCES

- Astropy Collaboration, Robitaille, T. P., Tollerud, E. J., et al. 2013, *A&A*, 558, A33, doi: [10.1051/0004-6361/201322068](https://doi.org/10.1051/0004-6361/201322068)
- Astropy Collaboration, Price-Whelan, A. M., Sipőcz, B. M., et al. 2018, *AJ*, 156, 123, doi: [10.3847/1538-3881/aabc4f](https://doi.org/10.3847/1538-3881/aabc4f)
- Astropy Collaboration, Price-Whelan, A. M., Lim, P. L., et al. 2022, *ApJ*, 935, 167, doi: [10.3847/1538-4357/ac7c74](https://doi.org/10.3847/1538-4357/ac7c74)
- Avdellidou, C., & Vaubaillon, J. 2019, *Astronomy & Astrophysics*, 626, A90, doi: [10.1051/0004-6361/201935396](https://doi.org/10.1051/0004-6361/201935396)
- Bottke, W. F., Moorhead, A. V., Connolly, H. C., et al. 2020, *Journal of Geophysical Research (Planets)*, 125, e06282, doi: [10.1029/2019JE006282](https://doi.org/10.1029/2019JE006282)
- Cervone, A., Topputo, F., Speretta, S., et al. 2022, *Acta Astronautica*, 195, 309, doi: [10.1016/j.actaastro.2022.03.032](https://doi.org/10.1016/j.actaastro.2022.03.032)
- Christiansen, E. L., Nagya, K., Lear, D. M., & Prior, T. G. 2009, Space station MMOD shielding, Pergamon
- Cipriano, A. M., Dei Tos, D. A., & Topputo, F. 2018, *Frontiers in Astronomy and Space Sciences*, 5, doi: [10.3389/fspas.2018.00029](https://doi.org/10.3389/fspas.2018.00029)
- Flynn, G. J., Nittler, L. R., & Engrand, C. 2016, *Elements*, 12, 177, doi: [10.2113/gselements.12.3.177](https://doi.org/10.2113/gselements.12.3.177)
- Gommers, R., Virtanen, P., Haberland, M., et al. 2025, `scipy/scipy`: SciPy 1.16.2, v1.16.2, Zenodo, doi: [10.5281/zenodo.17101542](https://doi.org/10.5281/zenodo.17101542). <https://doi.org/10.5281/zenodo.17101542>
- Grün, E., Zook, H. A., Fechtig, H., & Giese, R. H. 1985, *Icarus*, 62, 244, doi: [10.1016/0019-1035\(85\)90121-6](https://doi.org/10.1016/0019-1035(85)90121-6)
- Harris, C. R., Millman, K. J., van der Walt, S. J., et al. 2020, *Nature*, 585, 357, doi: [10.1038/s41586-020-2649-2](https://doi.org/10.1038/s41586-020-2649-2)
- Holsapple, K. A. 1993, *Annual Review of Earth and Planetary Sciences*, 21, 333, doi: [10.1146/annurev.ea.21.050193.002001](https://doi.org/10.1146/annurev.ea.21.050193.002001)
- Hunter, J. D. 2007, *Computing in Science & Engineering*, 9, 90, doi: [10.1109/MCSE.2007.55](https://doi.org/10.1109/MCSE.2007.55)
- Jessberger, E. K., Christoforidis, A., & Kissel, J. 1988, *Nature*, 332, 691, doi: [10.1038/332691a0](https://doi.org/10.1038/332691a0)
- Kereszturi, A. 2022, *Icarus*, 376, 148–179, doi: [10.1016/j.icarus.2021.114879](https://doi.org/10.1016/j.icarus.2021.114879)
- Love, S. G., & Brownlee, D. E. 1993, *Science*, 262, 550, doi: [10.1126/science.262.5133.550](https://doi.org/10.1126/science.262.5133.550)

- 674 Madiedo, J., Ortiz, J., Organero, F., et al. 2014, Icarus,
675 233, 27
- 676 McNamara, H., Jones, J., Kauffman, B., et al. 2004, Earth
677 Moon and Planets, 95, 123,
678 doi: [10.1007/s11038-005-9044-8](https://doi.org/10.1007/s11038-005-9044-8)
- 679 Melosh, H. J. 1989, Impact cratering: A geologic process,
680 Vol. 11 (Oxford University Press)
- 681 Moorhead, A. V. 2020, NASA Meteoroid Engineering
682 Model (MEM) Version 3, Tech. Rep. NTRS 20200000563,
683 NASA Meteoroid Environment Office
- 684 Moorhead, A. V., Clements, T. D., & Vida, D. 2020a,
685 MNRAS, 494, 2982, doi: [10.1093/mnras/staa719](https://doi.org/10.1093/mnras/staa719)
- 686 Moorhead, A. V., Kingery, A., & Ehlert, S. 2020b, Journal
687 of Spacecraft and Rockets, 57, 160, doi: [10.2514/1.A34561](https://doi.org/10.2514/1.A34561)
- 688 National Institute of Standards and Technology, PML.
689 2025, Composition of Nickel — NIST PML, <https://pml.nist.gov/cgi-bin/Star/compos.pl?matno=028>.
690 <https://pml.nist.gov/cgi-bin/Star/compos.pl?matno=028>
- 691 Peña-Asensio, E., Suñer, D., Gordo, S., & Cuesta, E. 2024,
692 Acta Astronautica, 219, 267,
693 doi: [10.1016/j.actaastro.2024.03.048](https://doi.org/10.1016/j.actaastro.2024.03.048)
- 694 Ryan, S., & Christiansen, E. L. 2010, Micrometeoroid and
695 orbital debris (MMOD) shield ballistic ... https://www.lpi.usra.edu/lpi/contribution_docs/LPI-001804.pdf
- 698 Ryan, S., Christiansen, E. L., Ordonez, E., & Lear, D. M.
699 2015, Hypervelocity Impact Performance of Open Cell
700 Foam Core Sandwich Panel Structures, Tech. Rep.
- 701 NASA/TM-2015-218593, NASA Johnson Space Center /
702 USRA / MEI Technologies
- 703 Smith, D. E., Zuber, M. T., Neumann, G. A., et al. 2010,
704 Geophysical Research Letters, 37, L18204,
705 doi: [10.1029/2010GL043751](https://doi.org/10.1029/2010GL043751)
- 706 Speyerer, E., Robinson, M., Boyd, A., Denevi, B., &
707 Wagner, R. 2016a, Nature, 538, 215
- 708 Speyerer, E. J., Povilaitis, R. Z., Robinson, M. S., Thomas,
709 P. C., & Wagner, R. V. 2016b, Nature, 538, 215–218,
710 doi: [10.1038/nature19829](https://doi.org/10.1038/nature19829)
- 711 Van Rossum, G., & Drake, F. L. 2009, Python 3 Reference
712 Manual (Scotts Valley, CA: CreateSpace)
- 713 Virtanen, P., Gommers, R., Oliphant, T. E., & et al. 2020a,
714 Nature Methods, 17, 261, doi: [10.1038/s41592-019-0686-2](https://doi.org/10.1038/s41592-019-0686-2)
- 715 Virtanen, P., Gommers, R., Oliphant, T. E., et al. 2020b,
716 Nature Methods, 17, 261, doi: [10.1038/s41592-019-0686-2](https://doi.org/10.1038/s41592-019-0686-2)
- 717 Wagg, T., Broekgaarden, F., & Gültkin, K. 2025,
718 TomWagg/software-citation-station: v1.3, v1.3, Zenodo,
719 doi: [10.5281/zenodo.1714520](https://doi.org/10.5281/zenodo.1714520).
- 720 <https://doi.org/10.5281/zenodo.1714520>
- 721 Wagg, T., & Broekgaarden, F. S. 2024, arXiv e-prints,
722 arXiv:2406.04405. <https://arxiv.org/abs/2406.04405>